Three-wave mixing traveling-wave parametric amplifier with periodic variation of the circuit parameters

Applied Physics Letters

Three-wave mixing traveling-wave parametric amplifier with periodic variation of the circuit parameters

Cite as: Appl. Phys. Lett. **122**, 052601 (2023); https://doi.org/10.1063/5.0127690
Submitted: 23 September 2022 • Accepted: 11 January 2023 • Published Online: 30 January 2023

Anita Fadavi Roudsari, Daryoush Shiri, Hampus Renberg Nilsson, et al.

AIP Publishing

Applied Physics Letters ARTICLE scitation.org/journal/apl

Three-wave mixing traveling-wave parametric amplifier with periodic variation of the circuit parameters

Cite as: Appl. Phys. Lett. **122**, 052601 (2023); doi: 10.1063/5.0127690
Submitted: 23 September 2022 · Accepted: 11 January 2023 ·
Published Online: 30 January 2023

Anita Fadavi Roudsari,[a] Daryoush Shiri, Hampus Renberg Nilsson, Giovanna Tancredi, Amr Osman, Ida-Maria Svensson, Marina Kudra, Marcus Rommel, Jonas Bylander, Vitaly Shumeiko, and Per Delsing

AFFILIATIONS

Department of Microtechnology and Nanoscience, Chalmers University of Technology, 412 96 Gothenburg, Sweden

[a]Author to whom correspondence should be addressed: fadavi@chalmers.se

ABSTRACT

We report on the implementation of a near-quantum-limited, traveling-wave parametric amplifier that uses three-wave mixing (3WM). To favor amplification by 3WM, we use superconducting nonlinear asymmetric inductive element (SNAIL) loops, biased with a dc magnetic flux. In addition, we equip the device with dispersion engineering features to create a stopband at the second harmonic of the pump and suppress the propagation of the higher harmonics that otherwise degrade the amplification. With a chain of 440 SNAILs, the amplifier provides up to 20 dB gain and a 3-dB bandwidth of 1 GHz. The added noise by the amplifier is found to be less than one photon.

Over six decades have passed since the first proposals on traveling-wave parametric amplifiers (TWPAs).[1–3] Since then, TWPAs have been widely used in optics;[4,5] however, in electronics and microwave circuits, they gave way to transistor-based amplifiers. Recent progress in superconducting quantum computing and the demand for quantum-limited amplifiers has brought the attention back to the TWPAs. Being composed of passive, low-loss elements such as capacitors and inductors, TWPAs are inherently low noise. This makes them ideal for millikelvin measurements. Furthermore, embedding the elements in a transmission-line frame liberates TWPAs from the constraint of a fixed gain-bandwidth product inherent in parametric amplifiers based on lumped element oscillators and resonators.[6,7]

Parametric amplification results from frequency mixing in a nonlinear element, where a strong pump is mixed with the weak signal, causing energy transfer from the pump to the signal and, thus, amplification. There are two main schemes of frequency mixing, namely, three-wave mixing (3WM) and four-wave mixing (4WM). 4WM-TWPAs appeared earlier and progressed both in the form of kinetic-inductance-based transmission lines[8–12] and of lumped-element circuits composed of Josephson junctions.[13–18] There are fewer implementations of 3WM-TWPAs,[19–25] despite the abundance of the theoretical work.[2,19,26–30]

The quadratic nonlinearity in a 3WM-TWPA leads to a greater amplification at lower pump powers compared with a 4WM-TWPA, which relies on cubic nonlinearity. This translates into a shorter chain for the 3WM-TWPA to achieve a target amplification,[26] which in turn introduces less loss to the system. Moreover, in a 3WM-TWPA, maximum amplification is close to half of the pump frequency, in contrast to a 4WM-TWPA, where the gain is maximum near the pump frequency. Therefore, the strong pump that is detuned from the signal can be filtered out easily. Furthermore, the 3WM-TWPA is not greatly affected by the intrinsic phase mismatch induced by the Kerr effect, which was believed to eliminate the need for dispersion engineering. In practice, however, the linear dispersion facilitates the generation of higher pump harmonics and up-converted signal modes. Therefore, the desired gain may not be achieved unless one increases the number of device unit cells.[29,31] This problem has so far been addressed by adding features to the TWPA chain to deliberately distort the linear dispersion and increase the phase mismatch at higher frequencies while maintaining finely tuned phase matching for a particular pump frequency. Although this approach results in gain enhancement, it suffers from the limited flexibility of the amplification band.[20,24]

Our proposed solution to the problem of high harmonic generation is creating a stopband for the second harmonic of the pump, $2\omega_p$, thus suppressing the generation and propagation of all pump

harmonics. This is similar to an approach for the 4WM-kinetic-inductance TWPAs,[8–10] where a stopband is used to suppress the third harmonic of the pump. A strong nonlinear dispersion in the vicinity of the stopband would also prevent upconversion of the signal and idler by the pump. Therefore, we anticipate a better amplifier performance as well as improved flexibility in adjusting the pump frequency compared to other proposals.[20,24,27]

We use the periodic loading method[32] and modify the chain inductance to create a distributed filter, resulting in a stopband at the frequency of $2\omega_p$. Such a filter is in the form of nonlinear inductor-capacitor (LC) cells, and besides frequency elimination, it contributes to the gain. Moreover, the design is free from additional sources of reflection and loss present in resonator-based dispersion engineering. With this design, we demonstrate up to 20 dB gain with a TWPA that contains only 440 LC cells.

The TWPA is illustrated in Fig. 1(a). The nonlinearity results from the Josephson junctions, arranged in the form of a superconducting nonlinear asymmetric inductive element (SNAIL) loop[33] to provide 3WM. The equivalent SNAIL inductance, L, is periodically modulated such that the three consecutive cells form a *supercell*, $L_1 - L_1 - L_2$, with $L_2 = (3/2)L_1$ being the loaded feature. We choose the capacitance C such that the supercell, as a whole, is impedance matched.[32] (Variation in the TWPA impedance with magnetic flux is insignificant at the frequencies of interest well below the stopband.) In general, one can place the loaded feature periodically after any number of L_1-cells and use a different capacitance, $C_2 \neq C$.

The SNAILs are configured with a single junction with Josephson energy E_{J1} and three identical junctions, each with energy E_{J2}, $E_{J1}/E_{J2} = \alpha = 0.16$. The normalized SNAIL inductive energy is then[33]

$$\frac{E_S(\tilde{\phi})}{E_{J2}} = -\alpha\cos(\tilde{\phi} + \tilde{\phi}_{min}) - 3\cos\left(\frac{\phi_{ext} - (\tilde{\phi} + \tilde{\phi}_{min})}{3}\right) \approx c_0\tilde{\phi}_{min} + c_2\tilde{\phi}^2 + c_3\tilde{\phi}^3 + c_4\tilde{\phi}^4 + \cdots, \quad (1)$$

where $\tilde{\phi}(t)$ is the phase difference across the SNAIL. The second line is an expansion of the energy around the minimum superconducting phase difference, $\tilde{\phi}_{min}$, defined by the biasing magnetic flux, $\phi_{ext} = 2\pi\Phi_{ext}/\Phi_0$. Equation (1) contains both third- and fourth-order nonlinear terms for the phase fluctuation, which are responsible for the 3WM and 4WM, respectively.

The dispersion relation is obtained by calculating the supercell transmission ($ABCD$) matrix, $\hat{\mathcal{M}}$, and solving the equation, $2\cosh(\gamma a) = \mathrm{Tr}(\hat{\mathcal{M}})$, where γ is the complex propagation constant and a is the length of the supercell.[32] Figure 1(b) shows the dispersion relation where the wave number k is the imaginary part of γ. The plot consists of three propagation bands separated by two stop-bands. The stop-bands variation with magnetic flux is illustrated in Fig. 1(c). The stopbands shift downwards in frequency as the magnetic flux approaches $0.5\,\Phi_0$, as the SNAIL inductance increases.

To account for the nonlinear coupling of the waves, we resort to a dynamical equation for the superconducting phase, $\phi(x,t)$, representing the n-th node of the chain at $x = na$. For a homogeneous chain, $L_2 = L_1$, the equation has the form[31]

$$-CL_1\ddot{\phi} - 4\sin^2\left(\frac{a\hat{k}}{2}\right)\phi + \frac{\chi_3}{2}\hat{\mathcal{D}}_3[\phi] + \frac{\chi_4}{3}\hat{\mathcal{D}}_4[\phi] = 0, \quad \hat{\mathcal{D}}_\mu[\phi] = \left[(1 - e^{-ia\hat{k}})\phi\right]^{\mu-1} - \left[(e^{ia\hat{k}} - 1)\phi\right]^{\mu-1}, \quad (2)$$

where $\hat{k} = -i\partial_x$ and the nonlinearity coefficients $\chi_3 = -3c_3/c_2$ and $\chi_4 = -6c_4/c_2$ quantify the strength of the 3WM and 4WM, respectively. Figure 1(d) shows the dependence of these coefficients on the magnetic flux. The 4WM coefficient χ_4 vanishes at $\Phi_{ext} \approx 0.36\,\Phi_0$. The χ_3-coefficient at this point is close to its maximum value. For the loaded TWPA, the dynamical description is more complex: one has to resolve the nodal phases within the supercell, $n = 3m$, $3m+1$, and $3m+2$, where m is the supercell number. Then Eq. (2) splits into three coupled equations for the corresponding phases (cf. Ref. 31). Nevertheless, Eq. (2) remains useful for the loaded chain as a tool for the qualitative description of a low-frequency region below the first stopband. Furthermore, in the long-wavelength limit, $ka \ll 1$ ($\omega \ll \omega_c$) and one can simplify Eq. (2) by the Taylor expansion over the small parameter ka.

We fabricated the device on a high resistivity silicon wafer ($\rho \geq 10\,\mathrm{k\Omega\,cm}$) with evaporated aluminum as the superconducting material, aluminum/aluminum oxide/aluminum (Al/AlO$_x$/Al) Josephson junctions, and parallel plate capacitors with amorphous

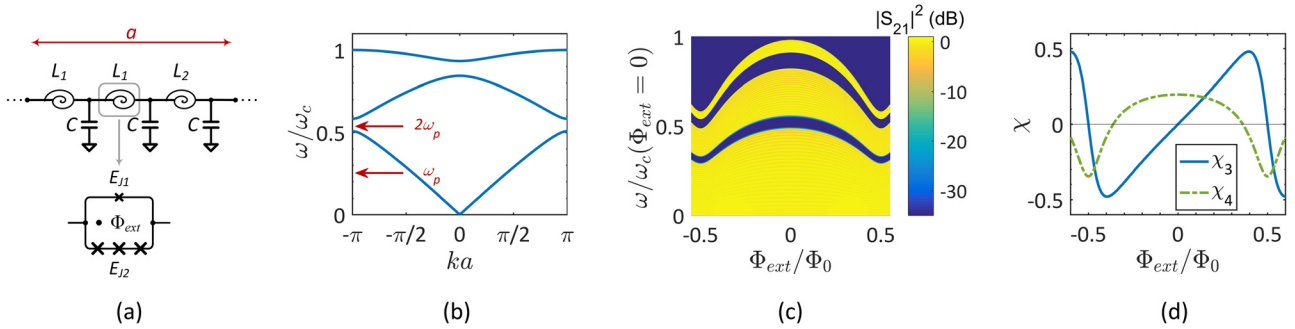

FIG. 1. Design of a stopband by periodic loading in the TWPA chain. (a) A supercell made of three SNAIL loops with inductances L_1, $L_2 = (3/2)L_1$. The SNAILs loop area is 40 μm^2, $E_{J1}/E_{J2} = 0.16$, $Ic_{J1} = 0.27$ μA, and $a = 45$ μm. (b) Calculated dispersion diagram of the device; the pump frequency ω_p is chosen such that its second harmonic is within the stopband. The stopbands are independent of magnetic flux when the frequency is normalized by the cutoff frequency, $\omega_c(\Phi_{ext})$. (c) Calculated transmission of the TWPA as a function of the frequency and magnetic flux, Φ_{ext}. The frequency is normalized by $\omega_c(\Phi_{ext} = 0)$. (d) Calculated nonlinearity coefficients χ_3 and χ_4 as a function of Φ_{ext}.

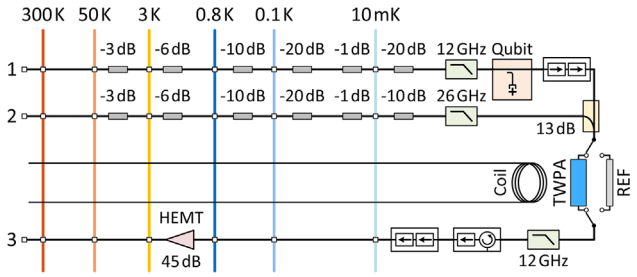

FIG. 2. Cryogenic measurement setup. The qubit chip contains a fixed-frequency transmon qubit ($f_q = 4.164$ GHz) connected to a readout resonator ($f_r = 6.0351$ GHz), used for measuring the input power at the chip.

aluminum nitride dielectric. We mounted a $5 \times 10\,\mathrm{mm}^2$ TWPA chip, containing 440 cells or ≈ 147 supercells, in a copper box and attached the assembly to the mixing chamber of a Bluefors dilution refrigerator to measure the device at temperatures around 10 mK. Figure 2 shows the wiring diagram of the cryogenic measurement setup. To apply the dc magnetic flux, we placed a superconducting coil under the sample. To calibrate the measurement, we used a 50 Ω SMA cable as the reference, marked with REF in the figure. The TWPA and the reference were connected to RF switches to share the input/output lines. The signal and the pump were fed through line 1 and line 2, respectively. They combined in a directional coupler before entering the TWPA. This was made to protect a qubit, accessible via the signal line, from being perturbed by the strong pump. We used this qubit to calibrate the power, allowing us to measure the noise temperature, as discussed later. During gain measurements, we combined the signal and the pump at room temperature and fed both through line 2.

We present the gain for pump frequencies between 7 and 8.4 GHz in Fig. 3 (blue, green, and purple traces). For each pump frequency, we kept the pump second harmonic within the stopband; thus, we changed the flux bias from $0.34\,\Phi_0$ down to $0.21\,\Phi_0$. Simultaneously, we ramped up the pump power not to decrease the ratio of the pumping current to the critical current. The gain increases with the growing pump frequency, following the theory prediction,[2,31] as the gain coefficient is proportional to the wave number of the pump. The gain maximum increases from ≈15 dB with the pump frequency of 7 GHz to about 20 dB within the pump frequency interval 7.8–8.4 GHz. At the same time, the shape of the gain traces does not change, indicating that 3WM remains dominant within the range of the applied magnetic bias, despite the increasing 4WM admixture. The frequency shift of the gain peak from half of the pump frequency is due to phase mismatch.[2,24,31] In Fig. 3, we also present the gain of a SNAIL-TWPA that contains no dispersion-engineering features (yellow trace). The latter was made of the same number of 440 SNAILs with similar configurations and measured at the same operational point. The clear difference in the frequency dependence and the level of the gain of the loaded TWPA indicate the effect of the suppression of high harmonics.

To investigate how effective the suppression by the stopband was, we probed the generation of the second harmonic of an injected mode. We biased the TWPA at $\approx 0.38\,\Phi_0$, where the stopband was accessible by our measurement setup and 4WM was negligible. We sent in a tone at frequency ω and power −111 dBm and measured the output signals at ω and 2ω using a spectrum analyzer. The experimentally measured transmission results are shown in Fig. 4. Each result is plotted after subtracting the measurement taken at zero flux instead of the reference cable to exclude the effect of the insertion loss. The response of the tone itself (blue) reveals the stopband starting at approximately 11.5 GHz. However, the second harmonic (green) does not change significantly in the stopband. This surprising observation, the absence of the extinction of the second harmonic, is confirmed by numerical simulation (yellow and purple dashed–dotted lines). The amplitude of the second harmonic in the stopband is approximately 10 dB smaller than the maximum below the stopband edge, whereas the main tone decreases by orders of magnitude. The simulation was performed using the harmonic-balance method implemented in the advanced design system simulator.[34] This method accounts for the full nonlinear dynamics of the Josephson inductance in response to the applied ac current and magnetic flux and returns all inter-mixing products generated in the circuit.

The difference in the behavior of the main tone and its second harmonic in the stopband can be understood by considering the nonlinear wave interactions. The second harmonic continuously interacts, even within the stopband, with the main tone, which freely propagates

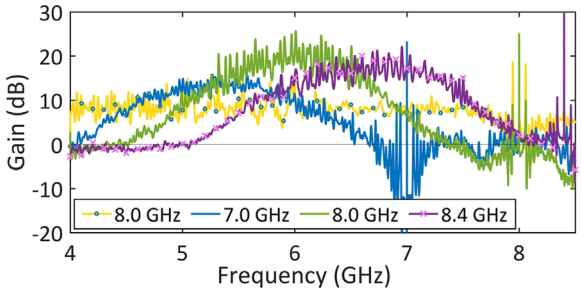

FIG. 3. Gain of the loaded TWPA at different pump frequencies (blue, green, and purple traces). For each trace, the flux is tuned to keep the second harmonic of the pump in the stopband. The pump power is also adjusted following the increase in the critical current with flux. Blue: $\Phi_{ext} = 0.34\,\Phi_0$, $P_p = -87.4$ dBm; green: $\Phi_{ext} = 0.22\,\Phi_0$, $P_p = -82.25$ dBm, purple: $\Phi_{ext} = 0.21\,\Phi_0$, $P_p = -82.4$ dBm. Yellow shows the gain of a TWPA without loading ($L_2 = L_1$). $\Phi_{ext} = 0.35\,\Phi_0$, $P_p = -89.4$ dBm.

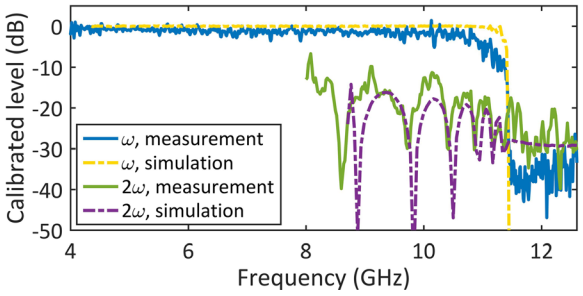

FIG. 4. Frequency response of the TWPA to an input tone with power −111 dBm at $\approx 0.38\,\Phi_0$. The response at the input frequency (blue) exhibits a stopband at $\gtrsim 11.5$ GHz, where the transmission drops by several orders of magnitude. The green trace shows the response at 2ω (the second harmonic corresponding to the range of 4 GHz $\leq \omega/2\pi \leq$ 6.25 GHz). It also drops within the stopband, but not as significantly as the main tone. The yellow and purple dashed–dotted lines indicate the simulation results described in the text.

at smaller frequencies within the propagating band and provides energy to the second harmonic. This understanding is supported by an analytical study of a simplified model for a TWPA with a stopband. The model reveals that the second harmonic (with frequency 2ω) contains a propagating part with a wave vector $2ik(\omega)$, in addition to an evanescent part with complex wave vector of the second harmonic $\gamma(2\omega)$. Once the evanescent term vanishes, the amplitude of the propagating wave becomes independent of the position in the TWPA chain. The amplitude of the wave is inversely proportional to the width of the stopband.

The observed small suppression of the second harmonic in the stopband illustrates a general property of the nonlinear media—the absence of the full extinction of a wave in a stopband due to nonlinear wave interactions.

We further investigated the presence of the (down-converted) idler, $\omega_i = \omega_p - \omega_s$, and the up-converted modes $(\omega_p + \omega_{s,i})$, for a signal within the interval 0.1–6.2 GHz. We biased the device at $\Phi \approx 0.38\,\Phi_0$ and applied the pump at 6.2 GHz so that its second harmonic was in the stopband. We used a spectrum analyzer and measured the response between 3.5–12.5 GHz, as shown in Fig. 5(a). The blue trace indicates the response at the signal frequency, ω_s, while the yellow depicts the idler, ω_i, when the signal is applied below 2.7 GHz. The green and purple traces represent the upconversion of the signal and idler, respectively, $\omega_p + \omega_{s,i}$. The peak at frequencies between 6.2 and 9 GHz indicates efficient upconversion from the quasi-linear dispersion region below 3 GHz. The significantly weaker response at frequencies above 9 GHz reveals the increased phase mismatch close to the stopband. Therefore, we conclude that the shape of the gain in Fig. 5(a) is mainly formed by an interplay of the three modes, ω_s, ω_i, and $\omega_p + \omega_{s(i)}$, Fig. 5(b).

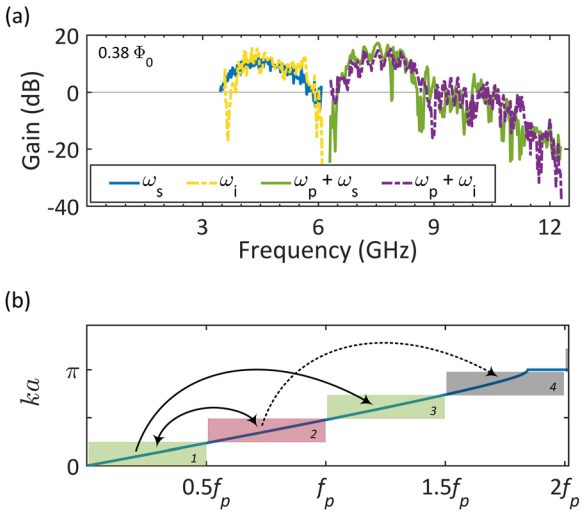

FIG. 5. (a) Frequency dependence of the output signal and 3WM idlers of the loaded TWPA, $\omega_p/2\pi = 6.2$ GHz, pump power, $P_p = -90.4$ dBm. The signal is injected between 0.1 and 6.2 GHz. (b) Frequency diagram illustrating mode coupling: the modes within frequency intervals 1 and 2 are strongly coupled by downconversion and, therefore, amplified. The modes within interval 1 are efficiently up-converted to region 3 above the pump frequency; however, this process does not result in amplification on its own. The modes within region 2 are not up-converted because of a large phase mismatch in the vicinity of the stopband (region 4, lower half) and suppression inside the stopband (region 4, upper half).

Our concluding discussion is about the noise performance of the TWPA. Figure 6(a) presents the noise temperature as a function of the gain, where the data points correspond to four close values of the magnetic flux bias $\Phi_{ext} \approx 0.2\,\Phi_0$. The input signal was calibrated by measuring the number of photons in the readout resonator of the qubit chip, see Fig. 2, via the ac Stark shift measurement.[35,36] Figure 6(a) also depicts the improvement of the signal-to-noise ratio (ΔSNR) defined as the ratio of the SNRs for the pump on and off. The noise temperature of the system is about 10 K when the TWPA is connected but not pumped, and drops to less than 0.6 K when the TWPA is pumped. To analyze the data, we adopt a model for the TWPA as an ideal amplifier with gain G, connected to a lossy element with damping D on the input,[37] see the inset of Fig. 6(b). The added number of noise photons referred to the TWPA input is

$$A(G) = \frac{1-D}{2D} + \frac{G-1}{2GD}. \tag{3}$$

The first term results from the damping, and the second is due to the gain, assuming the standard quantum limit.[38] Despite the phenomenological nature of the adopted model, it qualitatively captures the form of the added quantum noise due to the losses in the large gain limit.[39] The total system noise of the TWPA connected in series to the HEMT amplifier is

$$N_{tot}(G) = N_{in} + \frac{G(2-D)-1}{2GD} + \frac{A_H}{GD}. \tag{4}$$

Here, N_{in} and A_H are the input noise and the added noise by the HEMT amplifier, respectively, in units of noise photons. The second term is the noise added by the TWPA. The signal-to-noise ratio improvement is then

$$\Delta\mathrm{SNR}(G) = \frac{N_{in} + A(1) + \dfrac{A_H}{D}}{N_{in} + A(G) + \dfrac{A_H}{GD}}. \tag{5}$$

We fit the data in Fig. 6(a) using Eqs. (4) and (5), solid lines in the plots. Assuming vacuum input noise, we extract the parameters, $D = 0.73$ and $A_H = 24.85$. Note that D is comparable with the value of 0.79 that we obtain from the insertion loss measurement. We use D to compute the added noise of the TWPA, Eq. (3), as shown in Fig. 6(b). The saturated value of the added noise at large pump power is found, $A_\infty = 0.86$ photons. Thus, the added noise by TWPAs is only 0.36 photons above the standard quantum limit of $A_{SQL} = 0.5$.[38]

In summary, we demonstrated an enhanced gain in a Josephson junction-based TWPA in the three-wave-mixing regime, once we reduced the undesired effect of higher mode generation. Using periodic loading, we engineered a stopband in the frequency spectrum of the TWPA. We demonstrated that placing the stopband at twice the pump frequency suppressed the propagation of the second harmonic of the pump and the up-converted signal and idler. However, due to nonlinear interactions, the stopband did not fully eliminate these modes. Nevertheless, even with 10 dB suppression of the second harmonic of the pump, the maximum gain of the loaded TWPA is about 10 dB larger than that of a device with no dispersion engineering. A TWPA with a small number of 147 supercells shows a maximum gain of 20 dB, a 3-dB bandwidth of ≈1 GHz between 4 and 8 GHz, and an added noise below one photon. The width

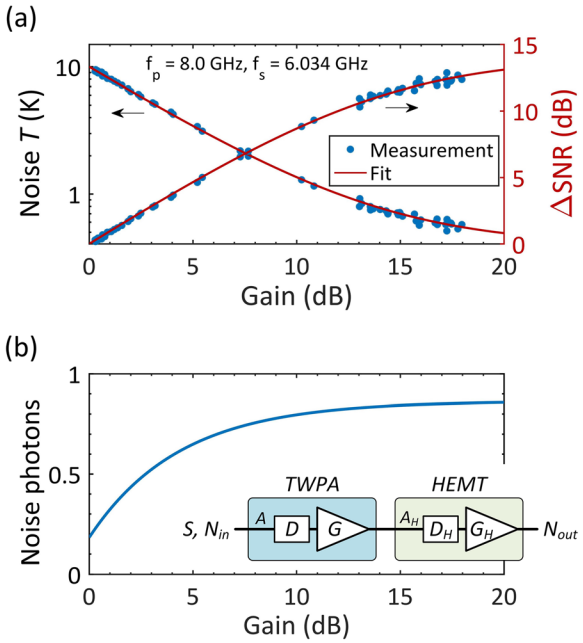

FIG. 6. Noise performance of the TWPA. (a) Noise temperature and the signal-to-noise ratio improvement of the system. (b) Added noise photons as a function of the gain. Inset: modeling the TWPA as an ideal amplifier connected to a lossy element, used to make the fit in (a).

of the stopband provides the flexibility of tuning the pump frequency over a range of 1.4 GHz, while the maximum gain remains above 15 dB.

This research was funded by the Knut and Alice Wallenberg Foundation through the Wallenberg Center for Quantum Technology (No. WACQT KAW 2021.0009) and by the EU Flagship on Quantum Technology (No. H2020-FETFLAG-2018-03) Project 820363 OpenSuperQ. The authors are grateful to Christian Fager for valuable advice on device modeling. The authors acknowledge the use of the Nanofabrication Laboratory (NFL) at Chalmers University of Technology. The authors are thankful for the support from Marco Scigliuzzo, Andreas Bengtsson, Yong Lu, Liangyu Chen, Hangxi Li, Christopher Warren, David Niepce, Eleftherios Moschandreou, Philip Krantz, and Lars Jönsson.

AUTHOR DECLARATIONS

Conflict of Interest

The authors have no conflicts to disclose.

Author Contributions

Anita Fadavi Roudsari: Conceptualization (lead); Data curation (lead); Formal analysis (equal); Investigation (equal); Writing – original draft (lead); Writing – review & editing (equal). **Vitaly Shumeiko:** Formal analysis (equal); Investigation (equal); Writing – original draft (equal); Writing – review & editing (equal). **Per Delsing:** Formal analysis (equal); Project administration (lead); Supervision (equal); Writing – review & editing (equal). **Daryoush Shiri:** Conceptualization (equal); Formal analysis (equal); Investigation (equal); Resources (equal); Writing – review & editing (equal). **Hampus Renberg Nilsson:** Data curation (equal); Resources (equal); Writing – review & editing (equal). **Giovanna Tancredi:** Data curation (equal); Formal analysis (supporting); Writing – review & editing (equal). **Amr Osman:** Data curation (supporting); Resources (supporting); Writing – review & editing (equal). **Ida-Maria Svensson:** Data curation (supporting); Writing – review & editing (equal). **Marina Kudra:** Data curation (supporting); Writing – review & editing (supporting). **Marcus Rommel:** Resources (supporting); Writing – review & editing (supporting). **Jonas Bylander:** Supervision (equal); Writing – review & editing (equal).

DATA AVAILABILITY

The data that support the findings of this study are available from the corresponding author upon reasonable request.

REFERENCES

[1]A. L. Cullen, "A travelling-wave parametric amplifier," Nature **181**, 332 (1958).
[2]P. K. Tien, "Parametric amplification and frequency mixing in propagating circuits," J. Appl. Phys. **29**, 1347 (1958).
[3]P. Tien and H. Suhl, "A traveling-wave ferromagnetic amplifier," Proc. IRE **46**, 700 (1958).
[4]P. Hedekvist, M. Karlsson, and P. Andrekson, "Fiber four-wave mixing demultiplexing with inherent parametric amplification," J. Lightwave Technol. **15**, 2051 (1997).
[5]P. Kylemark, H. Sunnerud, M. Karlsson, and P. A. Andrekson, "Semi-analytic saturation theory of fiber optical parametric amplifiers," J. Lightwave Technol. **24**, 3471 (2006).
[6]T. Yamamoto, K. Inomata, M. Watanabe, K. Matsuba, T. Miyazaki, W. D. Oliver, Y. Nakamura, and J. S. Tsai, "Flux-driven Josephson parametric amplifier," Appl. Phys. Lett. **93**, 042510 (2008).
[7]K. M. Sundqvist, S. Kintaş, M. Simoen, P. Krantz, M. Sandberg, C. M. Wilson, and P. Delsing, "The pumpistor: A linearized model of a flux-pumped superconducting quantum interference device for use as a negative-resistance parametric amplifier," Appl. Phys. Lett. **103**, 102603 (2013).
[8]B. Ho Eom, P. K. Day, H. G. LeDuc, and J. Zmuidzinas, "A wideband, low-noise superconducting amplifier with high dynamic range," Nat. Phys. **8**, 623 (2012).
[9]C. Bockstiegel, J. Gao, M. R. Vissers, M. Sandberg, S. Chaudhuri, A. Sanders, L. R. Vale, K. D. Irwin, and D. P. Pappas, "Development of a broadband NbTiN traveling wave parametric amplifier for MKID readout," J. Low Temp. Phys. **176**, 476 (2014).
[10]A. A. Adamyan, S. E. de Graaf, S. E. Kubatkin, and A. V. Danilov, "Superconducting microwave parametric amplifier based on a quasi-fractal slow propagation line," J. Appl. Phys. **119**, 083901 (2016).
[11]S. Chaudhuri, D. Li, K. D. Irwin, C. Bockstiegel, J. Hubmayr, J. N. Ullom, M. R. Vissers, and J. Gao, "Broadband parametric amplifiers based on nonlinear kinetic inductance artificial transmission lines," Appl. Phys. Lett. **110**, 152601 (2017).
[12]S. Goldstein, N. Kirsh, E. Svetitsky, Y. Zamir, O. Hachmo, C. E. M. de Oliveira, and N. Katz, "Four wave-mixing in a microstrip kinetic inductance travelling wave parametric amplifier," Appl. Phys. Lett. **116**, 152602 (2020).
[13]H. R. Mohebbi, "Parametric interaction in Josephson junction circuits and transmission lines," Ph.D. thesis (University of Waterloo, Waterloo, 2011).
[14]O. Yaakobi, L. Friedland, C. Macklin, and I. Siddiqi, "Parametric amplification in Josephson junction embedded transmission lines," Phys. Rev. B **87**, 144301 (2013).
[15]C. Macklin, K. O'Brien, D. Hover, M. E. Schwartz, V. Bolkhovsky, X. Zhang, W. D. Oliver, and I. Siddiqi, "A near–quantum-limited Josephson traveling-wave parametric amplifier," Science **350**, 307 (2015).
[16]T. C. White, J. Y. Mutus, I.-C. Hoi, R. Barends, B. Campbell, Y. Chen, Z. Chen, B. Chiaro, A. Dunsworth, E. Jeffrey *et al.*, "Traveling wave parametric amplifier

with Josephson junctions using minimal resonator phase matching," Appl. Phys. Lett. **106**, 242601 (2015).
[17]L. Planat, A. Ranadive, R. Dassonneville, J. Puertas Martínez, S. Léger, C. Naud, O. Buisson, W. Hasch-Guichard, D. M. Basko, and N. Roch, "Photonic-crystal Josephson traveling-wave parametric amplifier," Phys. Rev. X **10**, 021021 (2020).
[18]A. Ranadive, M. Esposito, L. Planat, E. Bonet, C. Naud, O. Buisson, W. Guichard, and N. Roch, "Kerr reversal in Josephson meta-material and traveling wave parametric amplification," Nat. Commun. **13**, 1737 (2022).
[19]A. B. Zorin, M. Khabipov, J. Dietel, and R. Dolata, "Traveling-wave parametric amplifier based on three-wave mixing in a Josephson metamaterial," in *Proceedings of* 2017 16th *International* Superconductive *Electronics Conference (ISEC)* (IEEE, 2017), pp. 1–3.
[20]M. R. Vissers, R. P. Erickson, H.-S. Ku, L. Vale, X. Wu, G. C. Hilton, and D. P. Pappas, "Low-noise kinetic inductance traveling-wave amplifier using three-wave mixing," Appl. Phys. Lett. **108**, 012601 (2016).
[21]L. Ranzani, M. Bal, K. C. Fong, G. Ribeill, X. Wu, J. Long, H.-S. Ku, R. P. Erickson, D. Pappas, and T. A. Ohki, "Kinetic inductance traveling-wave amplifiers for multiplexed qubit readout," Appl. Phys. Lett. **113**, 242602 (2018).
[22]A. Miano and O. A. Mukhanov, "Symmetric traveling wave parametric amplifier," IEEE Trans. Appl. Supercond. **29**, 1 (2019).
[23]S. Shu, N. Klimovich, B. H. Eom, A. D. Beyer, R. B. Thakur, H. G. Leduc, and P. K. Day, "Nonlinearity and wide-band parametric amplification in a (Nb, Ti)N microstrip transmission line," Phys. Rev. Res. **3**, 023184 (2021).
[24]M. Malnou, M. Vissers, J. Wheeler, J. Aumentado, J. Hubmayr, J. Ullom, and J. Gao, "Three-wave mixing kinetic inductance traveling-wave amplifier with near-quantum-limited noise performance," PRX Quantum **2**, 010302 (2021).
[25]M. Perelshtein, K. Petrovnin, V. Vesterinen, S. Hamedani Raja, I. Lilja, M. Will, A. Savin, S. Simbierowicz, R. Jabdaraghi, J. Lehtinen, L. Grönberg, J. Hassel, M. Prunnila, J. Govenius, G. Paraoanu, and P. Hakonen, "Broadband continuous variable entanglement generation using a Kerr-free Josephson metamaterial," Phys. Rev. Appl. **18**, 024063 (2022).
[26]A. B. Zorin, "Josephson traveling-wave parametric amplifier with three-wave mixing," Phys. Rev. Appl. **6**, 034006 (2016).
[27]R. P. Erickson and D. P. Pappas, "Theory of multiwave mixing within the superconducting kinetic-inductance traveling-wave amplifier," Phys. Rev. B **95**, 104506 (2017).
[28]A. Zorin, "Flux-driven Josephson traveling-wave parametric amplifier," Phys. Rev. Appl. **12**, 044051 (2019).
[29]T. Dixon, J. Dunstan, G. Long, J. Williams, P. Meeson, and C. Shelly, "Capturing complex behavior in Josephson traveling-wave parametric amplifiers," Phys. Rev. Appl. **14**, 034058 (2020).
[30]A. B. Zorin, "Quasi-phasematching in a poled Josephson traveling-wave parametric amplifier with three-wave mixing," Appl. Phys. Lett. **118**, 222601 (2021).
[31]H. Renberg Nilsson, A. Fadavi Roudsari, D. Shiri, P. Delsing, and V. Shumeiko, "A high gain travelling-wave parametric amplifier based on three-wave mixing," arXiv:2205.07758 [quant-ph] (2022).
[32]R. E. Collin, *Foundations for Microwave Engineering*, 2nd ed. (Wiley-IEEE Press, New York, 2001) pp. 550–647.
[33]N. E. Frattini, U. Vool, S. Shankar, A. Narla, K. M. Sliwa, and M. H. Devoret, "3-wave mixing Josephson dipole element," Appl. Phys. Lett. **110**, 222603 (2017).
[34]PathWave Advanced Design System (ADS) Software (2022).
[35]C. S. Macklin, "Quantum feedback and traveling-wave parametric amplification in superconducting circuits," Ph.D. thesis (University of California, Berkeley, 2015).
[36]A. Bruno, G. de Lange, S. Asaad, K. L. van der Enden, N. K. Langford, and L. DiCarlo, "Reducing intrinsic loss in superconducting resonators by surface treatment and deep etching of silicon substrates," Appl. Phys. Lett. **106**, 182601 (2015).
[37]C. Belove, *Handbook of Modern Electronics and Electrical Engineering* (Wiley, New York, 1986) pp. 1584–1585.
[38]C. M. Caves, "Quantum limits on noise in linear amplifiers," Phys. Rev. D **26**, 1817 (1982).
[39]M. Houde, L. Govia, and A. Clerk, "Loss asymmetries in quantum traveling-wave parametric amplifiers," Phys. Rev. Appl. **12**, 034054 (2019).